minerals

MDPI

Article

Effect of By-Product-Derived Low-Melting-Point Additive on Mineralogical and Metallurgical Properties of Iron Ore Sinter

Haeun Kim [1], In-kook Suh [1], Junyong Kim [2], Seung Seok Oh [2], In Ae Song [2], Jong-Hyup Lee [2,*] and Joonho Lee [1,*]

[1] Department of Materials Science and Engineering, Korea University, 145 Anam-ro, Seongbuk-gu, Seoul 02841, Republic of Korea
[2] Research & Development (R&D) Center, Hyundai Steel Company, 1480 Bukbusaneop-ro, Songak-eup, Dangjin-si, Chungcheongnam-do 31719, Republic of Korea
* Correspondence: rjh@hyundai-steel.com (J.-H.L.); joonholee@korea.ac.kr (J.L.)

Abstract

Reducing solid fuel consumption in iron ore sintering is an important strategy for lowering fossil fuel use and associated CO_2 emissions. However, insufficient heat input can limit liquid-phase formation and compromise sinter quality. In this study, a by-product-derived low-melting-point additive (LMA) was used under reduced-fuel sintering condition, and the resulting mineralogical characteristics, pore structural, and metallurgical properties were evaluated. Preformed Ca–Fe–O phases accounted for 46.2 wt.% of the quantified crystalline phase assemblage in the LMA. Differential scanning calorimetry revealed a thermal event near 1200 °C, interpreted as being associated with the onset of liquid-phase formation. In sinter pot tests, the LMA-containing reduced-fuel condition (RFL) exhibited a lower maximum bed temperature than the conventional reference condition (STD), decreasing from 1375 to 1339 °C. With the mean STD values normalized to 100%, the relative mean reducibility index, tumble index, and reduction disintegration index of RFL were 104.7%, 101.8%, and 100.3%, respectively, indicating that these quality indices remained broadly comparable despite the reduced fuel input. Rietveld refinement indicated a higher magnetite fraction and a lower SFCA-I fraction in RFL, suggesting that the higher mean reducibility could not be explained by bulk mineralogy alone. Optical microscopy of entire specimen cross-sections revealed a lower pore area fraction and a more consolidated structure in RFL, whereas mercury intrusion porosimetry indicated that mercury-accessible pore volume associated with pore-entry sized below 50 μm was largely maintained. Overall, these findings suggest that the combined use of LMA and reduced fuel input can maintain sinter quality at a lower maximum bed temperature. The pore-structure results provide a possible explanation for the higher mean reducibility despite the mineralogical changes, although a causal relationship has not been established.

Keywords: iron ore sinter; by-product; low-melting-point additive; calcium ferrite; reducibility; porosity

Check for updates

Academic Editor: Brajendra Mishra

Received: 22 September 2026
Revised: 6 November 2026
Accepted: 8 November 2026
Published: 13 November 2026

Copyright: © 2026 by the authors. Licensee MDPI, Basel, Switzerland. This article is an open access article distributed under the terms and conditions of the Creative Commons Attribution (CC BY) license.

1. Introduction

Iron ore sintering is a key agglomeration process for producing blast-furnace burden. Coke breeze supplies the heat required for partial melting and the formation of bonding phases during sintering. Reducing coke breeze consumption is therefore an important approach to decreasing fossil-fuel use and the associated CO_2 emissions. However, lower

fuel input can reduce the thermal level of the sinter bed, restrict melt formation, and consequently deteriorate sinter quality [1,2].

The mineralogical and metallurgical properties of sinter are closely related to the bonding phases and pore structure developed during sintering. Among these phases, silico-ferrite of calcium and aluminum (SFCA) and SFCA-I are key bonding phases that contribute to sinter strength and metallurgical performance [3]. Their formation and thermal stability are strongly influenced by temperature, oxygen partial pressure, and the concentrations of CaO, SiO_2, and Al_2O_3 [3–5]. Webster et al. [4] demonstrated that increasing the CaO/SiO_2 ratio broadened the thermal stability range of SFCA-I and promoted its formation. Increasing the Al_2O_3 content has also been reported to stabilize SFCA and SFCA-I over wider temperature ranges [6]. Ji et al. [7] showed that increasing the Al_2O_3 content could promote SFCA formation but decrease sinter strength at excessive Al_2O_3 levels, whereas increasing the SiO_2 content favored calcium silicate formation and suppressed SFCA development. These findings indicate that SFCA formation and liquid-phase generation are closely related but may respond differently to changes in oxide composition.

The melting and crystallization behavior of calcium ferrite-based bonding phases is particularly important because liquid-phase formation governs particle bonding and subsequent mineral development. Using in situ synchrotron X-ray diffraction, Webster et al. [6] reported that, during heating, SFCA formed at approximately 1107–1164 °C and decomposed to form a magnetite-containing melt assemblage at approximately 1213–1308 °C, depending on the composition of the synthetic mixtures investigated. During cooling, an Fe-rich phase crystallized from the melt and subsequently reacted with the remaining liquid to form SFCA. These observations show that SFCA formation involves both reactions during heating and liquid-assisted reactions during cooling, and that its thermal stability depends on composition. Park et al. [8] further investigated SFCA crystallization in the Fe_2O_3–CaO–SiO_2–Al_2O_3 system using in situ confocal laser scanning microscopy and showed that the Al_2O_3 content and cooling conditions influence phase development. Thus, the final bonding structure depends not only on liquid-phase formation during heating but also on subsequent phase transformations and crystallization during cooling.

One approach to compensate for reduced heat input is to promote melt formation at lower temperatures through the addition of calcium ferrite-based materials. Preformed calcium ferrites have been shown to facilitate low-temperature liquid-phase formation and modify pore development while maintaining sinter quality [2]. Calcium ferrite-based materials have also been produced from Fe- and Ca-bearing steelmaking by-products, highlighting their potential as low-melting-point binders for iron ore sintering [9]. In addition, Fe- and C-bearing residues, such as blast-furnace dust, can be recycled through the sintering process to partially replace conventional coke breeze [10]. Recent pilot-scale investigations have further demonstrated the feasibility of using calcium ferrite-based additives in sintering with reduced-fuel input [11]. Nevertheless, enhanced liquid-phase formation does not necessarily ensure favorable sinter properties, as the final mineral assemblage and pore structure also depend on thermal history and solidification behavior [3,6,12].

The effects of raw material composition and processing conditions on sintering performance are commonly evaluated using laboratory- or pilot-scale sinter pot tests. Honeyands et al. [13] investigated the relationship between basicity and sinter mineralogy by comparing industrial sinter samples with products from pilot-scale pot tests, laboratory-scale milli-pot tests, and sinter analog experiments. In conventional pot tests, the surface of a granulated raw material bed is ignited, and the combustion front propagates downward under induced airflow. Sintering performance is evaluated in terms of parameters such as burn-through time, sinter yield, and productivity, whereas product quality is commonly characterized by the tumble index (TI), reducibility index (RI), and reduction disintegration

index (RDI) [13]. Nicol et al. [14] demonstrated that coke breeze addition rate and draft pressure affect the temperature profile and oxygen partial pressure within the sinter bed, thereby influencing the resulting phase assemblages. Harvey et al. [15] further reported that, under their experimental conditions, the reducibility of sinter analogs was governed primarily by porosity rather than bonding-phase mineralogy. These findings highlight the importance of jointly evaluating thermal conditions, mineralogical composition, and pore structure when assessing sinter quality [12,14,15].

Collectively, these studies suggest that low-melting-point Ca–Fe–O materials and the recycling of ironmaking by-products offer potential routes to reducing fuel consumption in sintering [2,10,11]. However, the relationships among additive-assisted liquid-phase formation, mineral phase development, and pore structure under reduced-fuel pot-sintering conditions remain insufficiently understood, particularly with respect to sinter strength and reducibility. In the present study, a by-product-derived low-melting-point additive (LMA) was used in sintering with reduced fuel input. The mineralogical and thermal characteristics of the LMA were first examined, followed by sinter pot tests using a conventional reference blend (STD) and a reduced-fuel blend containing the LMA (RFL). This study aimed to determine whether sinter quality could be maintained at a lower maximum bed temperature through the use of the LMA under reduced-fuel conditions and to elucidate the relationships among phase formation, pore structure, and reducibility.

2. Materials and Methods

2.1. Raw Material Preparation and Low-Melting-Point Additive

The raw materials used in the sinter pot tests consisted of an industrial iron ore blend, fluxes, return fines, coke breeze, and a by-product-derived low-melting-point additive(LMA) in this study. The iron ore blend was prepared by mixing high-grade ore, medium-grade ore, and three types of low-grade ore in proportions appropriate for each operating condition. Silica sand, limestone, and quicklime were used as fluxes, while coke breeze was used as solid fuel. Return fines generated from the sintering process were also included in the raw material mixture.

The LMA was prepared and supplied by Hyundai Steel Company using two ironmaking-related industrial by-products: a Fe-rich by-product (BP-A) and a Ca-rich by-product (BP-B). The chemical compositions of these by-products, determined by X-ray fluorescence (XRF) analysis, together with their loss on ignition (LOI) and moisture contents, are presented in Table 1.

Table 1. Chemical compositions of the two industrial by-products used to prepare the LMA (wt.%).

Type	Chemical Composition (wt.%)											
	Fe_2O_3	CaO	SiO_2	Al_2O_3	MgO	MnO	K_2O	Na_2O	TiO_2	P_2O_5	LOI	$-H_2O$
BP-A	75.37	1.67	2.78	0.91	0.20	0.21	0.46	0.03	0.27	0.17	17.54	0.24
BP-B	2.38	50.29	2.74	1.36	1.34	0.07	0.33	<0.02	0.08	0.02	41.20	0.30

BP-A and BP-B were mixed at a mass ratio of 59:41 (BP-A:BP-B) and pelletized. The resulting pellets were heated to 1000 °C at a heating rate of 10 °C/min in a box furnace and calcined for 30 min. After calcination, the pellets were sieved to obtain particles in the 3–5 mm size range. The resulting material is hereafter referred to as the low-melting-point additive (LMA). The appearance of the calcined LMA particles is shown in Figure 1, and their chemical composition is presented in Table 2.



Figure 1. Appearance of the LMA (particle size: 3–5 mm).

Table 2. The chemical composition of LMA.

Material	Chemical Composition (wt.%)											
	T. Fe	CaO	SiO_2	Al_2O_3	MgO	MnO	K_2O	Na_2O	TiO_2	P_2O_5	C *	S *
LMA	48.10	37.90	6.67	3.30	1.44	0.14	0.72	0.12	0.19	0.29	1.34	0.30

***** C and S were separately determined by combustion analysis and are reported on an elemental basis. The other components were determined by X-ray fluorescence (XRF) analysis and are expressed as elemental Fe (T.Fe) or oxide equivalents. The combined values were not renormalized to 100 wt.%.

Two sinter blend conditions were investigated: a conventional reference blend, designated as STD, and an LMA-containing blend, designated as RFL. In RFL, LMA was added at 3 wt.% based on the fraction of the sinter blend excluding 25 wt.% return fines, corresponding to 2.25 wt.% of the total mixture. Also, the coke breeze charge was reduced by 1.75% relative to that used in STD. The raw material blending proportions were adjusted based on their chemical compositions to achieve a target basicity (CaO/SiO_2 mass ratio) of 2.0 for both STD and RFL blends. Two independent sinter pot tests were conducted for each condition. The detailed blend proportions of the raw materials of STD and RFL are given in Table 3.

Table 3. The blend proportions of the raw materials for pot tests.

Raw Materials	STD (wt.%)	RFL (wt.%)
Ore blend	59.10	58.31
Silica sand	0.11	0.13
Limestone	9.50	8.09
Quicklime	2.30	2.30
Coke breeze	4.00	3.93
Return fines	25.00	25.00
LMA	0	2.25

2.2. Sinter Pot Test and Evaluation of Sinter Quality

Sinter pot tests were conducted at Hyundai Steel Company using an industrial iron ore blend under two operating conditions: the conventional reference blend (STD) and the reduced-fuel blend containing 3 wt.% of the low-melting-point additive (RFL). The tests were performed in a cylindrical sinter pot with an internal diameter of 250 mm and a total depth of 750 mm.

The raw materials were mixed for 4 min using a drum mixer. Water was added during mixing according to the optimum moisture content predetermined for each blend. After adding water, granulation continued for 5 min using the drum mixer. The resulting green granules had an average particle size of approximately 3–4 mm.

After granulation, the green mix was charged into the sinter pot. Approximately 64.4 kg of granulated green mix was then charged to form a bed with a depth of 570 mm. Ignition was performed using a downward-fired LPG burner at 1100 °C for 105 s. A downward suction pressure of 1000 mmH_2O (approximately 9.8 kPa) was applied during ignition. After ignition, the suction pressure was increased to 1500 mmH_2O (approximately 14.7 kPa) and maintained throughout the main sintering period. The bed temperature was monitored using a thermocouple installed approximately at the middle height of the sinter bed. The maximum temperature recorded at this position during sintering was defined as the maximum sintering temperature.

Sintering progress and completion were monitored based on the waste-gas temperature. After completion of sintering, the sinter cake was discharged and cooled in air for approximately 1–2 h. The cooled cake was subsequently crushed using a jaw crusher and screened according to particle size. The fraction larger than 5 mm was classified as product sinter, whereas the fraction smaller than 5 mm was classified as return fines.

The bulk chemical compositions of the product sinters were determined by X-ray fluorescence spectroscopy (XRF), except for FeO, which was determined separately by wet chemical analysis.

The mechanical strength of the product sinter was evaluated using the tumble index (TI). A sinter sample weighing 15 kg with a particle-size range of 10–25 mm was charged into a tumbler and rotated for 200 revolutions. After tumbling, the sample was screened using a 6.3 mm sieve, and the mass of the fraction retained above 6.3 mm was measured. TI was calculated as follows:

$$\mathrm{TI}(\%) = \frac{W_{+6.3}}{W_0} \times 100 \quad (1)$$

where W_0 is the initial mass of the sinter sample before tumbling, and $W_{+6.3}$ is the mass of the fraction larger than 6.3 mm after tumbling.

The degree of reduction in the product sinter, hereafter referred to as the reducibility index (RI), was evaluated with reference to ISO 7215:2015 and JIS M 8713:2021 [16,17]. A 500 g sinter sample with a particle-size range of 15–20 mm was charged into a reaction tube. The sample was reduced at 900 °C for 180 min under a gas mixture containing 30 vol.% CO and 70 vol.% N_2 at a total flow rate of 15 L/min. The mass of the reduced sample was then measured. RI was calculated from the mass loss during reduction and the initial total Fe and FeO contents of the sinter using the following equation:

$$\mathrm{RI}(\%) = \frac{(W_0 - W_1)}{W_0(0.430A - 0.112B)} \times 10^4 \quad (2)$$

where W_0 is the mass of the sinter sample before reduction (g), W_1 is the mass of the sample after 180 min of reduction (g), A is the total Fe content of the unreduced sinter (%), and B is the FeO content of the unreduced sinter (%).

The low-temperature reduction disintegration behavior of the product sinter was evaluated with reference to JIS M 8720:2023 [18]. A 500 g sinter sample with a particle-size range of 15–20 mm was charged into a reaction tube and reduced at 550 °C for 30 min under a gas mixture containing 30 vol.% CO and 70 vol.% N_2 at a total flow rate of 15 L/min. The reduced sample was subsequently charged into a tumbler and rotated for 900 revolutions. After tumbling, the sample was screened using a 2.8 mm sieve, and the mass of the fraction

retained above 2.8 mm was measured. The reduction disintegration index, expressed as the mass percentage of particles smaller than 2.8 mm, was calculated as follows:

$$\mathrm{RDI}_{-2.8}(\%) = \frac{W_R - W_{+2.8}}{W_R} \times 100 \quad (3)$$

where W_R is the mass of the reduced sample before tumbling, and $W_{+2.8}$ is the mass of the fraction retained above the 2.8 mm sieve after tumbling.

The sinter pot tests and quality evaluations were conducted by Hyundai Steel Company, while the chemical, mineralogical, and microstructural analyses of the supplied product sinters were performed in the present study.

2.3. Characterization Methods

The thermal behavior of the LMA was examined by differential scanning calorimetric analysis (DSC) using an STA 449 F5 Jupiter simultaneous thermal analyzer (NETZSCH-Gerätebau GmbH, Selb, Germany). Approximately 200 mg of LMA powder was uniaxially compacted into a 10 mm-diameter tablet using a hydraulic press at 5 tons. A fragment weighing approximately 15–20 mg was subsequently taken from the compacted tablet and placed in an Al_2O_3 crucible for thermal analysis. The sample was heated from room temperature to 1450 °C at a heating rate of 10 °C/min under flowing synthetic air (21 vol.% O_2 and 79 vol.% N_2) at a total flow rate of 50 mL/min. An empty crucible of the same type was used as the reference. The DSC data were processed using NETZSCH Proteus software (v.6.1.0), and the onset and peak temperatures of the thermal events were determined using the built-in analysis functions. The measurement was repeated twice to confirm reproducibility.

The bulk chemical compositions of the product sinters STD and RFL were determined using an X-ray fluorescence spectrometer (XRF). The crystalline phases present in the prepared LMA and the product sinters STD and RFL were characterized by powder X-ray diffraction (XRD) using an Empyrean (Malvern Panalytical) equipped with Cu Kα radiation (λ = 1.5406 Å) and a PIXcel3D detector. Before analysis, the samples were crushed to below 75 μm. The measurements were performed at 45 kV and 40 mA over a 2θ range of 5–90° with a step size of 0.013° and a scanning rate of 0.5° min^{-1}.

Crystalline phases were initially identified by comparing the measured XRD patterns with reference diffraction data from the Inorganic Crystal Structure Database (ICSD), the ICDD Powder Diffraction File (PDF), and the Crystallography Open Database (COD). Quantitative phase analysis of STD and RFL was subsequently conducted by Rietveld refinement using HighScore Plus software (v.4.7a; Malvern Panalytical, Almelo, The Netherlands). The quality of each refinement was assessed using the weighted profile residual (R_{wp}) and the goodness-of-fit (GOF) value.

Prior to optical microscopy and SEM–EDS analysis, the specimens were mounted in resin and sequentially ground using SiC abrasive papers from 100 to 2000 grit. The ground specimens were then polished using diamond suspensions with particle sizes of 3, 1, and 0.25 μm, in sequence. Optical microscopy was performed using an optical microscope (AXIO LAB A1 MAT, Carl Zeiss Microscopy, Jena, Germany) equipped with a HAL 50 illumination system and a 5XHD objective lens. SEM–EDS analysis was performed using a field-emission scanning electron microscope (FE-SEM, SU5000, Hitachi High-Tech Corporation, Tokyo, Japan) equipped with an energy-dispersive X-ray spectroscopy detector (Ultim Max 40, Oxford Instruments NanoAnalysis, High Wycombe, UK). The SEM observations were conducted at an accelerating voltage of 15.0 kV. Before analysis, the specimens were coated with Platinum. Here, EDS results were used only to describe local compositional variations and to compare the measured ratios with nominal calcium ferrite stoichiometries.

For quantitative assessment of apparent porosity, optical micrographs of the product sinters were acquired at a total magnification of 50× and stitched to reconstruct the entire cross-section of each specimen. Pore regions were segmented using Adobe Photoshop. A common threshold was selected based on the contrast between the solid matrix and pore regions and applied consistently to all images. Resin-impregnated pores that could not be distinguished by thresholding alone were manually delineated and included in the total pore area, whereas resin outside the specimen boundary was excluded. The segmented images were subsequently analyzed using ImageJ (v.1.54). Apparent porosity was calculated as the ratio of the internal pore area to the total specimen cross-sectional area. Three cross-sectional images were analyzed for each experimental condition.

The pore-size distribution of the product sinters was characterized by mercury intrusion porosimetry (MIP) using an AutoPore V 9620 (MicUSA). The product sinter was crushed into fragments of approximately 10 mm, and 2.26–3.48 g of sample was used for each measurement. Two independent measurements were conducted for each condition.

3. Results and Discussion

3.1. Mineralogical and Thermal Characteristics of the Low-Melting-Point Additive

The mineralogical composition of the LMA was first characterized by XRD, and the identified crystalline phases were subsequently quantified by Rietveld refinement. As shown in Figure 2 and Table 4, the LMA consisted predominantly of Ca–Fe–O phases together with hematite, magnetite, and residual Ca-bearing phases. Four calcium ferrite-related phases were identified: $Ca_2Fe_2O_5$ (C2F), $CaFe_2O_4$ (CF), $CaFe_4O_7$ (CF2), and $CaFe_3O_5$ (CWF), with phase fractions of 21.5, 11.6, 10.5, and 2.6 wt.%, respectively. Thus, Ca–Fe–O phases accounted for 46.2 wt.% of the crystalline phase assemblage. Among these phases, C2F was the most abundant, followed by CF and CF2. The coexistence of several calcium ferrite phases therefore indicates that the LMA contains a substantial amount of preformed Ca–Fe–O reaction products rather than consisting solely of unreacted Ca- and Fe-bearing constituents.

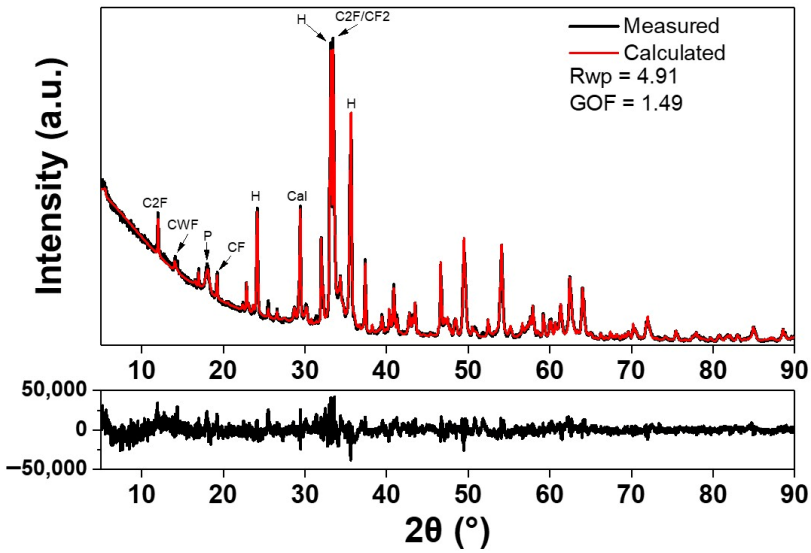


Figure 2. Measured and calculated XRD patterns of the LMA. C2F: $Ca_2Fe_2O_5$; CF: $CaFe_2O_4$; CF2: $CaFe_4O_7$; CWF: $CaFe_3O_5$; H: Fe_2O_3; P: $Ca(OH)_2$; Cal: $CaCO_3$.

Table 4. Quantitative phase composition of LMA determined by Rietveld refinement.

Phase	Chemical Formula	Phase Fraction (%)
C2F	$Ca_2Fe_2O_5$	21.5
CF	$CaFe_2O_4$	11.6
CF2	$CaFe_4O_7$	10.5
CWF	$CaFe_3O_5$	2.6
Hematite	Fe_2O_3	27.5
Magnetite	Fe_3O_4	4.7
Lime	CaO	4
Portlandite	$Ca(OH)_2$	8.4
Calcite	$CaCO_3$	7
Kalsilite	$KAlSiO_4$	1.4
Graphite	C	0.7

Hematite and magnetite accounted for 27.5 and 4.7 wt.%, respectively, corresponding to a combined iron-oxide fraction of 32.2 wt.%. Lime, portlandite, and calcite were also detected at 4.0, 8.4, and 7.0 wt.%, respectively. Although the LMA had undergone thermal treatment before use, the portlandite and calcite detected by XRD do not necessarily represent phases that remained unchanged during the thermal treatment. Free CaO generated during thermal treatment can hydrate upon exposure to atmospheric moisture, and the resulting $Ca(OH)_2$ can subsequently undergo carbonation in the presence of CO_2 [19,20]. Therefore, at least part of the detected $Ca(OH)_2$ and $CaCO_3$ may have formed during cooling, storage, or handling after thermal treatment. Minor amounts of kalsilite ($KAlSiO_4$, 1.4 wt.%) and graphite (0.7 wt.%) were also identified.

The microstructural and local chemical composition of the LMA were further examined using OM and SEM–EDS. As shown in Figure 3, the LMA exhibited a highly heterogeneous and porous microstructure. Numerous resin-impregnated pores, visible as the darkest regions in the BSE image (Figure 3b), were distributed throughout the solid matrix. To assess the representativeness of these observations, at least five LMA granules were examined, with multiple regions and EDS points investigated. Similar microstructural features and Ca–Fe-rich regions were observed in most of the areas examined. Representative regions and EDS analysis points are presented in Figure 4, and the corresponding compositions are summarized in Table 5.

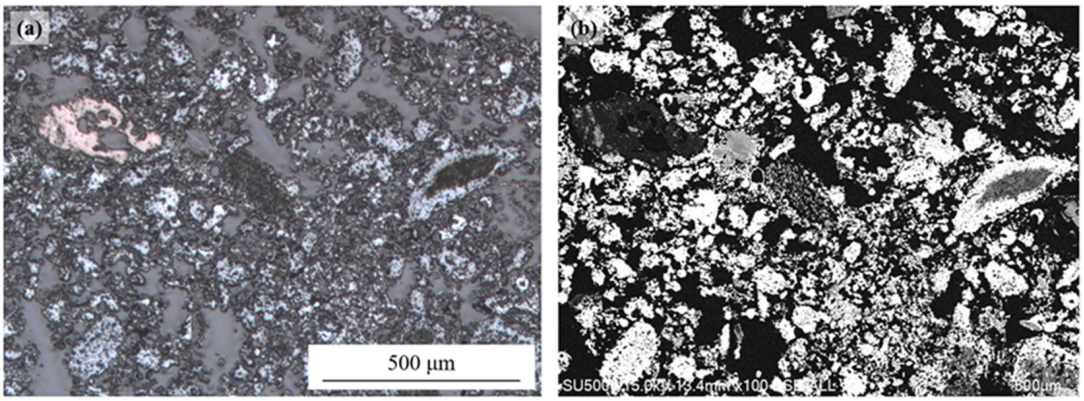


Figure 3. Representative cross-sectional microstructures of the LMA: (**a**) optical micrograph and (**b**) backscattered-electron SEM image.

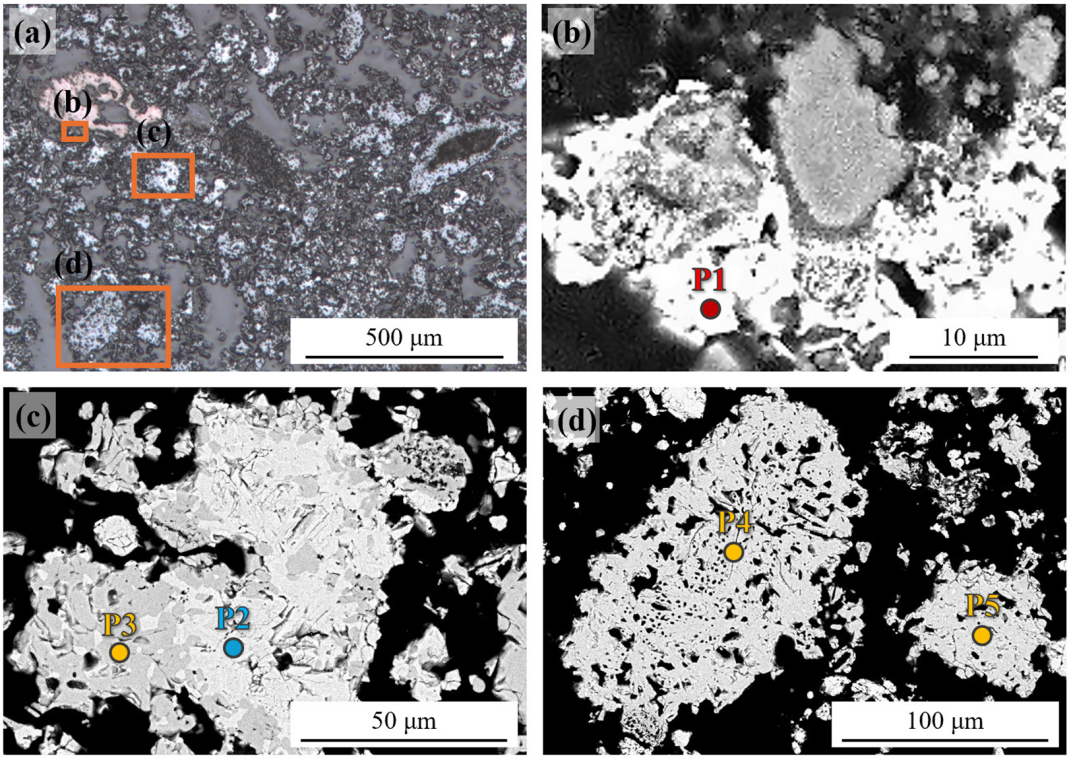


Figure 4. Microstructure and local compositions of calcium ferrite-rich regions in the LMA: (**a**) optical micrograph showing representative regions selected for SEM analysis; (**b**–**d**) enlarged SEM(BSE) images with EDS point-analysis locations. The red (P1), blue (P2), and yellow (P3–P5) markers indicate regions with Ca/Fe atomic ratios close to those of CF, CF2, and C2F, respectively.

Table 5. Representative elemental compositions and Ca/Fe atomic ratios of calcium ferrite-rich regions in the LMA determined by SEM–EDS.

Point	Element (at. %)							Ca/Fe
	C	O	Mg	Al	Si	Ca	Fe	
P1	26.24	43.69		3.67	0.24	8.19	17.97	0.46
P2	14.45	52.32	0.56			6.03	26.64	0.23
P3	16.38	50.28				16.43	16.9	0.97
P4	17.69	47.78				17.77	16.75	1.06
P5	14.61	50.46				17.36	17.56	0.99

The measured Ca/Fe atomic ratios ranged from 0.23 to 1.06. P1 showed a Ca/Fe atomic ratio of 0.46, close to the theoretical value of 0.50 for CF ($CaFe_2O_4$), whereas P2 exhibited a ratio of 0.23, close to the value of 0.25 for CF_2 ($CaFe_4O_7$). In contrast, P3–P5 exhibited ratios of 0.97–1.06, close to the stoichiometric value of 1.00 for C_2F ($Ca_2Fe_2O_5$). These differences indicate local variations in the relative proportions of Ca and Fe within the LMA. However, the relatively high carbon content measured at P1 (26.24 at.%) may partly reflect contributions from the mounting resin, introducing uncertainty into the EDS quantification. The Ca/Fe atomic ratios were therefore used to assess local compositional variations rather than to definitively identify individual calcium ferrite phases; phase identification was based primarily on XRD analysis with Rietveld refinement.

Taken together, the microstructural observations and XRD–Rietveld results suggest the coexistence of preformed Ca–Fe–O phases and reactive Ca-bearing constituents that may undergo further phase transformation during reheating. The thermal behavior of the

LMA was therefore subsequently investigated using DSC to examine characteristic thermal events and assess the onset of liquid-phase formation.

The thermal behavior of the LMA was subsequently examined by DSC to evaluate the reactions of the residual constituents and the onset of liquid-phase formation. A representative DSC curve is shown in Figure 5, while the onset temperatures obtained from two independent measurements are summarized in Table 6. Three characteristic thermal events were consistently observed.

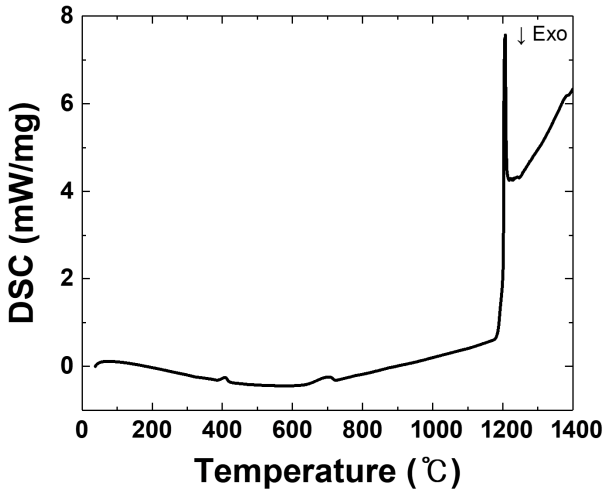


Figure 5. Representative DSC curve of the LMA during heating. The onset temperatures of the characteristic thermal events obtained from two independent measurements are summarized in Table 6.

Table 6. Onset temperatures of the characteristic thermal events observed during DSC analysis of the LMA.

Thermal Event		Onset Temperature (°C)	
		Run 1	Run 2
1st	Dehydration of $Ca(OH)_2$	389.0	416.5
2nd	Decarbonation of residual $CaCO_3$	650.4	653.3
3rd	Liquid formation	1201.9	1199.7

The first event occurred at approximately 389–417 °C and was attributed to the dehydration of residual portlandite ($Ca(OH)_2$). This event is consistent with the $Ca(OH)_2$ phase identified by Rietveld refinement, indicating that part of the residual Ca-bearing constituent dehydrated during reheating. A second thermal event occurred at approximately 650–653 °C and was assigned to decarbonation of residual calcite ($CaCO_3$). The close agreement between the two measurements for this event supports the presence of residual carbonate identified by XRD. The most pronounced high-temperature event occurred at approximately 1200 °C, with onset temperatures of 1199.7 and 1201.9 °C, respectively. This event was attributed to the onset of liquid-phase formation in the LMA. Considering the coexistence of preformed calcium ferrites, residual Fe-rich oxides, and reactive Ca-bearing phases revealed by XRD and SEM–EDS, the formation of liquid at this temperature is likely associated with further reactions among these constituents during heating.

Notably, the thermal event associated with liquid formation at approximately 1200 °C occurred below the typical peak temperature range of 1300–1480 °C reported for conventional iron ore sintering [21]. This observation suggests that the preformed Ca–Fe–O phases in the LMA may contribute to liquid-phase formation during reheating at lower temperatures when incorporated into a sinter mixture, potentially facilitating bonding reactions at

lower temperatures. Previous studies have similarly reported liquid formation near 1200 °C in calcium ferrite-containing systems and demonstrated that preformed calcium ferrites can facilitate melt formation at lower temperatures during sintering [2,22]. Thus, the LMA may serve not only as a source of Ca and Fe but also as a pre-reacted flux that promotes low-temperature liquid-phase formation during sintering.

3.2. Pot Performance and Quality of the Product Sinters

The chemical compositions of STD and RFL are summarized in Table 7, and the corresponding sinter quality indices and fuel ratio are compared in Figure 6. In RFL, the coke breeze charge was reduced by 1.75% relative to STD, while LMA was added to the blend. The maximum sintering temperature of the pot test decreased from 1375 °C for STD to 1339 °C for RFL, corresponding to a decrease of 36 °C. Despite the lower maximum bed temperature, the measured quality indices were maintained, while the mean RI was slightly higher for RFL than for STD. The mean RI showed a slight increase from 100% in STD to 104.7% in RFL. However, considering the overlapping standard deviations from duplicate tests, the reducibility index should be interpreted as being essentially maintained rather than distinctly enhanced. The TI also increased slightly from 100% to 101.8%, whereas the RDI remained essentially unchanged at 100% and 100.3% for STD and RFL, respectively. Thus, the higher reducibility of RFL was achieved without an apparent deterioration in mechanical strength or low-temperature reduction-disintegration behavior.

Table 7. Chemical compositions of the product sinters STD and RFL. The reported values represent the averages of two independently prepared samples for each condition ($n = 2$). FeO was determined by wet chemical analysis, whereas the remaining chemical components were measured by XRF.

Sample	Chemical Composition (wt. %)													C/S
	T.Fe	CaO	SiO_2	Al_2O_3	MgO	Na_2O	K_2O	TiO_2	V_2O_5	P_2O_5	Mn	ZnO	FeO	
STD	57.01	10.97	5.31	2.08	0.73	N.D.	0.08	0.12	0.01	0.13	0.07	N.D.	7.4	2.07
RFL	56.89	10.83	5.55	2.1	0.69	N.D.	0.08	0.12	0.01	0.14	0.07	0.01	7.69	1.95

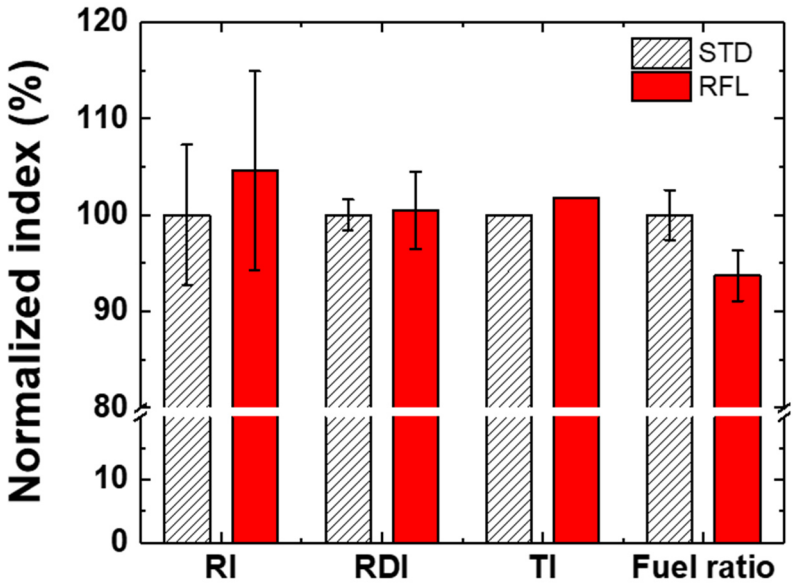


Figure 6. Normalized RI, RDI, TI, and fuel ratio of STD and RFL. Values are normalized to the corresponding values of STD (STD = 100%). Error bars represent the standard deviations of duplicate measurements for RI, RDI, and fuel ratio. TI was measured once.

Overall, RFL preserved the principal quality indices and maintained the reducibility of the product sinter under a reduced-fuel condition, despite the adverse bulk mineralogical shift. The simultaneous decrease in maximum sintering temperature and increase in RI indicates that the RFL condition, in which LMA addition was coupled with reduced fuel input, altered the mineralogical and/or pore-structural characteristics relevant to reduction. These changes are examined in the following section.

The reduced coke breeze input in RFL may also have environmental implications. Coke breeze is a major solid fuel used in iron ore sintering, and its combustion contributes to process CO_2 emissions [1]. Previous studies have shown that preformed calcium ferrites can facilitate sintering at lower temperatures while maintaining sinter quality, potentially reducing coke breeze consumption [2,11]. Jiang et al. [23] also reported reductions in solid-fuel consumption and measured CO_2 emissions per tonne of sinter following coke breeze modification in sinter pot experiments. Although the LMA contained residual carbon (1.34 wt.%), the coke breeze input in RFL was 1.75% lower than that in STD. This decrease indicates a potential reduction in CO_2 emissions associated with coke breeze consumption but does not demonstrate a net reduction in overall process emissions.

3.3. Mineralogical and Pore-Structural Characteristics of Product Sinters

The phase compositions of STD and RFL were quantified by Rietveld refinement, as shown in Figure 7 and Table 8. Both samples consisted mainly of hematite, magnetite, SFCA, and SFCA-I. The hematite fraction remained nearly unchanged from 23.4% in STD to 23.7% in RFL, whereas magnetite increased from 15.9 to 22.0% and SFCA-I decreased from 46.1 to 38.3%. SFCA remained constant at 9.4%, while larnite increased slightly from 4.4 to 5.8%.

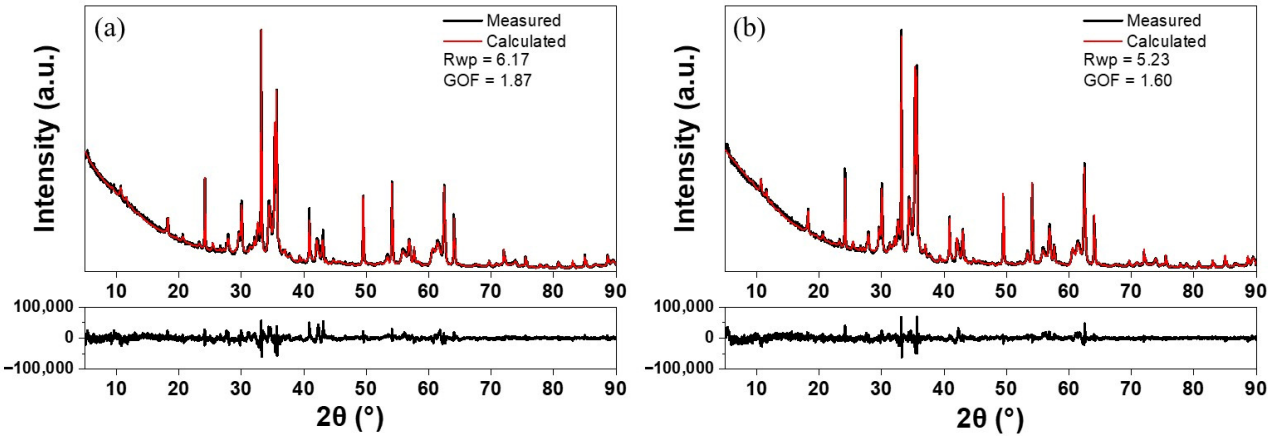


Figure 7. Measured and calculated XRD patterns obtained by Rietveld refinement for (**a**) STD and (**b**) RFL.

Table 8. Quantitative phase fractions of STD and RFL determined by Rietveld refinement.

Sample	Calculated Phase Fraction (%)						
	Hematite	Magnetite	SFCA	SFCA-I	Larnite	Wüstite	Quartz
STD	23.40	15.90	9.40	46.10	4.40	0.50	0.30
RFL	23.7	22.00	9.40	38.30	5.80	0.50	0.30

The increase in magnetite accompanied by the decrease in SFCA-I reflects the integrated response of the combined LMA-assisted reduced-fuel condition-involving lower peak temperature, reduced solid fuel, and slightly lower basicity-rather than an isolated metallurgical effect of LMA addition alone. One possible factor contributing to the lower

SFCA-I fraction is the difference in basicity between the two product sinters. The C/S ratio slightly decreased from 2.07 in STD to 1.95 in RFL. In situ diffraction studies have demonstrated that increasing basicity expands the thermal stability range of SFCA-I and increases the amount of SFCA-I formed [4]. Consistently, plant- and pot-scale sinter studies have shown that lower-basicity sinters tend to contain higher proportions of magnetite, whereas increasing basicity promotes the formation of calcium-ferrite bonding phases [13]. Thus, although the difference in basicity between STD and RFL was relatively small, its effect is directionally consistent with the lower SFCA-I and higher magnetite fractions observed in RFL.

The final balance between magnetite and calcium-ferrite phases is also strongly affected by the local oxygen potential and the subsequent reoxidation behavior during cooling. Controlled-atmosphere studies have shown that lower oxygen potentials favor the retention of magnetite and suppress the formation of calcium-ferrite bonding phases [5,24]. In particular, SFCA-I was not observed at an oxygen partial pressure of 1×10^{-4} atm, whereas both SFCA-I and SFCA formed under more oxidizing conditions [5]. Moreover, magnetite formed at high temperature can react with oxygen and the surrounding melt during cooling to form hematite and calcium-ferrite bonding phases; conversely, magnetite is retained when this reoxidation is limited [24]. Quenched sinter-pot studies have similarly shown that magnetite and melt dominate near the flame front, whereas calcium-ferrite phases develop predominantly during subsequent cooling [25].

In the present study, the FeO content was slightly higher in RFL (7.69 wt.%) than in STD (7.40 wt.%). Although this difference is qualitatively consistent with greater retention of Fe^{2+}-bearing phases, it is insufficient by itself to establish a difference in local oxygen potential because the redox atmosphere within the bed was not directly measured. Therefore, the higher magnetite and lower SFCA-I contents of RFL may reflect the combined effects of its slightly lower basicity and differences in the formation and reoxidation of Fe-bearing phases during the thermal cycle. The lower maximum bed temperature may also have modified the overall reaction history, but temperature alone is unlikely to account for the observed decrease in SFCA-I.

Despite these mineralogical changes, the RI of RFL was higher than that of STD. Hematite and Ca-ferrite-bearing phases are generally more reducible than magnetite [12], while SFCA-I has been reported to be more readily reduced than SFCA because of differences in their crystal structures [26]. Therefore, the higher RI of RFL cannot be explained by the bulk phase composition alone. This suggests that pore-structural characteristics relevant to reducing gas accessibility also played an important role, as discussed below.

Figure 8 compares representative whole-section OM images of STD and RFL, selected from specimens with apparent porosities closest to the mean value of each condition. The mean apparent porosity was lower in RFL ($27.88 \pm 5.20\%$) than in STD ($35.56 \pm 2.47\%$) as shown in Figure 9, and the RFL cross-section exhibited a more consolidated matrix with fewer large visible voids. This change is consistent with the low-temperature liquid-forming characteristics of the LMA. As discussed in Section 3.1, the LMA contained preformed Ca–Fe–O phases and exhibited a thermal event associated with incipient liquid formation at approximately 1200 °C. Previous studies have shown that preformed calcium ferrites can lower the required sintering temperature and shift the dominant pore structure from macropores toward medium and micropores [2]. The more consolidated structure of RFL may therefore have contributed to the slightly higher TI observed for RFL.

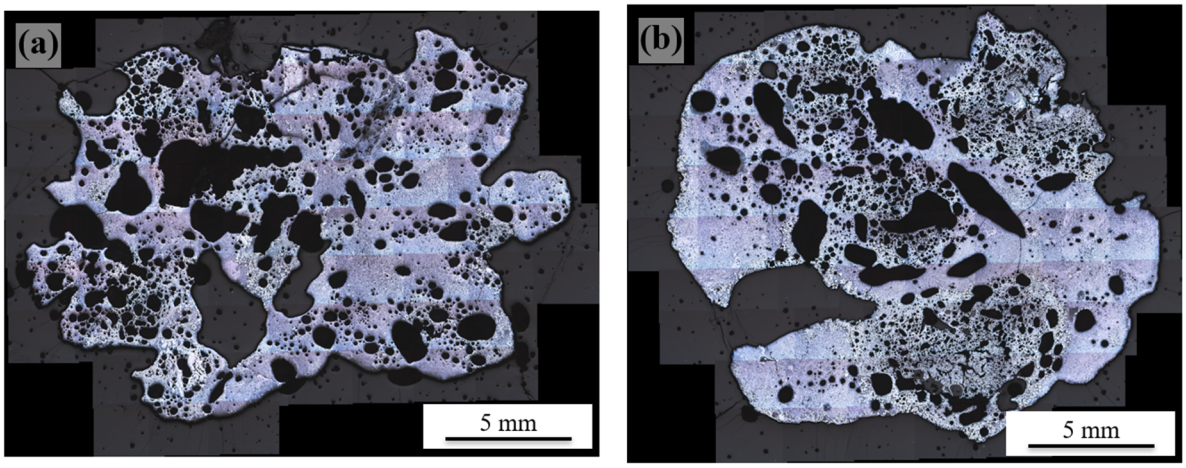


Figure 8. Representative whole-section optical micrographs of product sinters: (**a**) STD and (**b**) RFL. The images were selected from specimens exhibiting apparent porosities closest to the mean value of each condition.

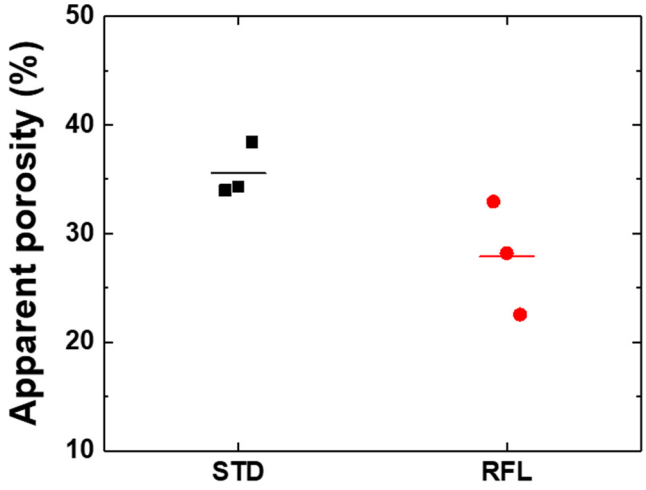


Figure 9. Apparent porosity determined from cross-sectional OM images. Individual measurements are shown as symbols, and horizontal lines indicate the mean values.

The MIP results are presented in Figure 10. Despite the lower mean apparent porosity measured by OM, the mercury-accessible pore volume below 50 μm was broadly retained in RFL across the 10–50 μm, 1–10 μm, 0.1–1 μm, and <0.1 μm ranges. OM and MIP provide complementary information: OM reflects the two-dimensional area of visible pore bodies, whereas MIP characterizes mercury-accessible pores and is strongly influenced by pore entrances and constrictions. Thus, the decrease in apparent porosity did not necessarily correspond to an equivalent loss of the accessible internal pore structure.

Pore accessibility is important for sinter reduction because open and interconnected pores provide pathways for reducing gases to reach internal mineral grains [27]. Previous studies have shown that porosity can strongly influence overall reducibility, and that substantial differences in mineral phase fractions do not necessarily result in corresponding differences in reducibility when the pore structure is comparable or favorable [12,28]. Although the bulk mineralogy shifted unfavorably toward higher magnetite and lower SFCA-I contents, the retention of mercury-accessible pores(<50 μm) in RFL appears to have preserved sufficient reducing gas permeability. This indicates that the accessible micropore network can compensate for unfavorable phase assemblages, thereby preventing the deterioration of overall reducibility.

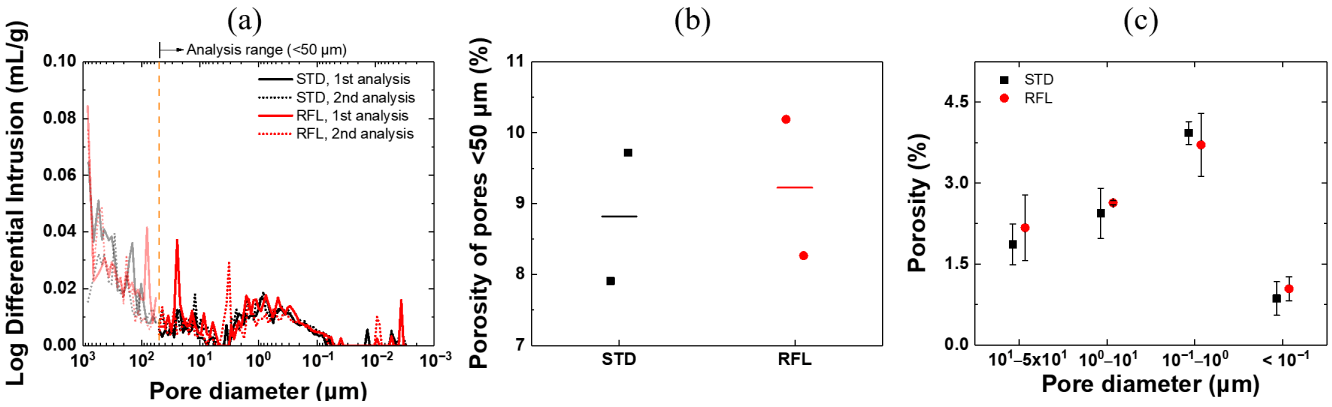


Figure 10. Mercury intrusion porosimetry results for STD and RFL: (**a**) log differential intrusion as a function of pore diameter, (**b**) porosity below 50 μm, and (**c**) porosity classified by pore diameter range. Individual measurements are shown in (**a**) and (**b**); horizontal lines in (**b**) indicate the mean values. Error bars in (**c**) represent the standard deviations of duplicate measurements.

4. Conclusions

In this study, we investigated the mineralogical and thermal characteristics of a by-product-derived low-melting-point additive (LMA) and its application under reduced-fuel sintering conditions. The principal findings are summarized as follows.

(1) The LMA contained a substantial fraction of preformed Ca–Fe–O phases, including C2F, CF, CF2, and CWF, which together accounted for 46.2 wt.% of the quantified crystalline phase assemblage. DSC analysis showed a reproducible high-temperature thermal event at approximately 1200 °C, which was attributed to incipient liquid-phase formation. These results indicate that the LMA is a pre-reacted Ca–Fe-bearing material with the potential to facilitate liquid formation at relatively low temperatures.

(2) Under the RFL condition, in which LMA addition was coupled with reduced solid-fuel input, the maximum bed temperature decreased from 1375 to 1339 °C. Despite the lower temperature, the mean RI was comparable or slightly higher (100% to 104.7%), and the TI remained equivalent (100% and 101.8%, single-run determination). Thus, the investigated product quality indices were maintained under the reduced-fuel, lower-temperature condition.

(3) The mineralogical assemblage of RFL shifted toward a higher magnetite fraction and a lower SFCA-I fraction. Magnetite increased from 15.9 to 22.0%, whereas SFCA-I decreased from 46.1 to 38.3%. This redistribution cannot be attributed to LMA addition alone because the RFL condition simultaneously involved reduced fuel input and a slightly lower product basicity. The observed changes are consistent with the combined effects of basicity, thermal history, and the formation and reoxidation behavior of Fe-bearing phases during sintering.

(4) Whole-section optical image analysis showed a lower mean apparent porosity and a more consolidated structure with fewer large visible voids in RFL. In contrast, MIP analysis showed that mercury-accessible pores below 50 μm were broadly retained. The combination of a more consolidated macroscopic structure and retained fine-to-intermediate mercury-accessible pores may have contributed to maintaining mechanical strength while preserving gas access during reduction.

Overall, the results show that, under the investigated conditions, the LMA-assisted reduced-fuel approach lowered the maximum bed temperature while maintaining the evaluated sinter quality indices and producing a higher mean RI. The lower coke breeze input also reduced the fossil-carbon input to the sintering process, suggesting the potential for

lower fuel-related CO_2 emissions during sintering. The use of an additive derived from iron-making by-products provides an additional resource-recycling benefit. The maintenance of reducibility despite the decrease in SFCA-I highlights that preserving gas-accessible fine-to-intermediate pores can offset adverse bulk phase shift in lower-temperature, reduced-fuel sintering operations. Because LMA addition and fuel reduction were not independently varied, their individual contributions cannot be separated from the present results. Further work incorporating independently controlled operating conditions, direct flue-gas measurements, carbon-balance analysis, and assessment of emissions associated with LMA production and raw materials is required to quantify the respective effects of the LMA and fuel reduction and evaluate the net CO_2 reduction potential of the overall process.

Author Contributions: Conceptualization, J.L.; methodology, J.L.; software, H.K.; validation, H.K. and I.-k.S.; formal analysis, H.K.; investigation, H.K., J.K., S.S.O., I.A.S., J.-H.L.; resources, J.-H.L.; data curation, H.K. and J.K.; writing—original draft preparation, H.K.; writing—review and editing, J.L. and I.-k.S.; visualization, H.K.; supervision, J.L.; project administration, J.-H.L. and J.L.; funding acquisition, J.-H.L. and J.L. All authors have read and agreed to the published version of the manuscript.

Funding: This work was supported by the Korea Planning & Evaluation Institute of Industrial Technology (KEIT) and the Ministry of Trade, Industry & Energy (MOTIE, Korea) of the Republic of Korea (No. RS-2024-00431460, No. RS-2026-25528538) and by the Korea Institute of Energy Technology Evaluation and Planning (KETEP) and the Ministry of Climate, Energy & Environment (MCEE) of the Republic of Korea (No. RS-2024-00401917).

Data Availability Statement: The data presented in this study are available on request from the corresponding author. The raw data are not publicly available due to commercial restrictions.

Conflicts of Interest: Authors Junyong Kim, Seung Seok Oh, In Ae Song, and Jong-Hyup Lee were employed by the Hyundai Steel Company. The remaining authors declare that the research was conducted in the absence of any commercial or financial relationships that could be construed as a potential conflict of interest.

References

1. Mohammad, S.; Patra, S.; Harichandan, B. Reductants in iron ore sintering: A critical review. *Fuel* **2023**, *332*, 126194. [CrossRef]
2. da Rocha, L.T.; Cho, S.; Kim, S.-W.; Jung, S.-M. Effects of adding iron ores-based calcium ferrites to the sinter mix on sinter quality and reduction of CO_2, NO and SO_2. *ISIJ Int.* **2022**, *62*, 2587–2598. [CrossRef]
3. Nicol, S.; Chen, J.; Pownceby, M.I.; Webster, N.A.S. A review of the chemistry, structure and formation conditions of silico-ferrite of calcium and aluminum ('SFCA') phases. *ISIJ Int.* **2018**, *58*, 2157–2172. [CrossRef]
4. Webster, N.A.S.; Pownceby, M.I.; Madsen, I.C.; Studer, A.J.; Manuel, J.R.; Kimpton, J.A. Fundamentals of silico-ferrite of calcium and aluminum (SFCA) and SFCA-I iron ore sinter bonding phase formation: Effects of CaO/SiO_2 ratio. *Metall. Mater. Trans. B* **2014**, *45*, 2097–2105. [CrossRef]
5. Webster, N.A.S.; Pownceby, M.I.; Madsen, I.C.; Kimpton, J.A. Effect of oxygen partial pressure on the formation mechanisms of complex Ca-rich ferrites. *ISIJ Int.* **2013**, *53*, 774–781. [CrossRef]
6. Webster, N.A.S.; Pownceby, M.I.; Madsen, I.C.; Kimpton, J.A. Silico-ferrite of calcium and aluminum (SFCA) iron ore sinter bonding phases: New insights into their formation during heating and cooling. *Metall. Mater. Trans. B* **2012**, *43*, 1344–1357. [CrossRef]
7. Ji, Z.; Zhao, Y.; Gan, M.; Fan, X.; Chen, X.; Hu, L. Microstructure and minerals evolution of iron ore sinter: Influence of SiO_2 and Al_2O_3. *Minerals* **2019**, *9*, 449. [CrossRef]
8. Park, T.J.; Choi, J.S.; Min, D.J. Influence of Al_2O_3 content and cooling rate on crystallization in Fe_2O_3–CaO–SiO_2–Al_2O_3 systems. *Met. Mater. Int.* **2022**, *28*, 2033–2041. [CrossRef]
9. Park, S.H.; Chu, Y.S.; Seo, S.K.; Park, J.W. The properties of synthetic calcium ferrite for ironmaking and steelmaking using industrial by-products—(1). *Resour. Recycl.* **2014**, *23*, 3–11. [CrossRef]
10. Lanzerstorfer, C.; Bamberger-Strassmayr, B.; Pilz, K. Recycling of blast furnace dust in the iron ore sintering process: Investigation of coke breeze substitution and the influence on off-gas emissions. *ISIJ Int.* **2015**, *55*, 758–764. [CrossRef]

11. da Rocha, L.T.; Cho, S.; Kim, S.-W.; Chung, B.-J.; Jung, S.-M. Development of a low-carbon sintering process technology and its application to a pilot-scale sintering testing. *ISIJ Int.* **2024**, *64*, 1871–1880. [CrossRef]
12. Ignácio, I.R.; Brooks, G.; Pownceby, M.I.; Rhamdhani, M.A.; Rankin, W.J.; Webster, N.A.S. Porosity, mineralogy, strength, and reducibility of sinter analogues from the Fe_2O_3(Fe_3O_4)-CaO-SiO_2 (FCS) ternary system. *Minerals* **2022**, *12*, 1253. [CrossRef]
13. Honeyands, T.; Nguyen, T.B.T.; Pinson, D.; Connolly, P.R.J.; Pownceby, M.I.; Manuel, J.; Matthews, L.; Leedham, J.; Singh, T.; O'Dea, D.P. Variation in Iron Ore Sinter Mineralogy with Changes in Basicity. *Minerals* **2022**, *12*, 1249. [CrossRef]
14. Nicol, S.; Chen, J.; Qi, W.; Mao, X.; Jak, E.; Hayes, P.C. Measurement of process conditions present in pilot scale iron ore sintering. *Minerals* **2019**, *9*, 374. [CrossRef]
15. Harvey, T.; Pownceby, M.I.; Chen, J.; Webster, N.A.S.; Nguyen, T.B.T.; Matthews, L.; O'Dea, D.; Honeyands, T. Effect of temperature, time, and cooling rate on the mineralogy, morphology, and reducibility of iron ore sinter analogues. *JOM* **2021**, *73*, 345–355. [CrossRef]
16. *ISO 7215:2015*; Iron Ores for Blast Furnace Feedstocks—Determination of the Reducibility by the Final Degree of Reduction Index. ISO: Geneva, Switzerland, 2015.
17. *JIS M 8713:2021*; Iron Ores—Determination of Reducibility by the Final Degree of Reduction Index. JSA: Tokyo, Japan, 2021.
18. *JIS M 8720:2023*; Iron Ores—Determination of Low-Temperature Reduction-Disintegration. JSA: Tokyo, Japan, 2023.
19. Maciel-Camacho, A.; Rodríguez Hernández, H.; Hills, A.W.D.; Morales, R.D. Hydration Kinetics of Lime. *ISIJ Int.* **1997**, *37*, 468–476. [CrossRef]
20. Erans, M.; Nabavi, S.A.; Manović, V. Carbonation of Lime-Based Materials under Ambient Conditions for Direct Air Capture. *J. Clean. Prod.* **2020**, *242*, 118330. [CrossRef]
21. Park, J.; Kim, E.; Suh, I.-K.; Lee, J. A Short Review of the Effect of Iron Ore Selection on Mineral Phases of Iron Ore Sinter. *Minerals* **2022**, *12*, 35. [CrossRef]
22. Guo, H.; Guo, X.-M. Effect of alumina on liquid phase formation in sintering process of iron ore fines. *Steel Res. Int.* **2019**, *90*, 1900138. [CrossRef]
23. Jiang, W.; Zhong, Q.; Teng, F.; Liu, J.; Gao, Z.; Yin, H.; Fan, L.; Xu, B.; Rao, M.; Peng, Z. A Fuel Modification Strategy for Cleaner Iron Ore Sintering: Lime Milk-Derived Calcium Oxide Coating of Coke Breeze for Combustion Regulation and Multi-Pollutant Reduction. *J. Clean. Prod.* **2026**, *574*, 149051. [CrossRef]
24. Hsieh, L.-H.; Whiteman, J.A. Effect of Oxygen Potential on Mineral Formation in Lime-Fluxed Iron Ore Sinter. *ISIJ Int.* **1989**, *29*, 625–634. [CrossRef]
25. van den Berg, T.; de Villiers, J.P.R.; Cromarty, R.D. Variation of the Redox Conditions and the Resultant Phase Assemblages during Iron Ore Sintering. *Int. J. Miner. Process.* **2016**, *150*, 47–53. [CrossRef]
26. Maruoka, D.; Mataoka, S.; Kasai, E.; Murakami, T. Influence of Crystal Structure and Chemical Composition on the Reducibility of Silico-Ferrite of Calcium and Aluminum in CO–CO_2–H_2–H_2O Atmosphere. *ISIJ Int.* **2024**, *64*, 795–802. [CrossRef]
27. Maeda, T.; Ono, Y. Experimental Study on the Relation between Microstructures of Constituent Minerals and Pores and Reducibility of Sinter. *Tetsu-to-Hagané* **1986**, *72*, 775–782. [CrossRef] [PubMed]
28. Barustan, M.I.A.; Copland, E.; Nguyen, T.B.T.; Jenkins, D.R.; O'Dea, D.; Honeyands, T. Reducibility of Iron Ore Sinter Analogues under Hydrogen-Enriched and Conventional Blast Furnace Gas Compositions. *ISIJ Int.* **2026**, *66*, 313–324. [CrossRef]

Disclaimer/Publisher's Note: The statements, opinions and data contained in all publications are solely those of the individual author(s) and contributor(s) and not of MDPI and/or the editor(s). MDPI and/or the editor(s) disclaim responsibility for any injury to people or property resulting from any ideas, methods, instructions or products referred to in the content.